International Journal of Engineering

Optimization of Operating Parameters of a Scroll Expander Based on Response Surface and NSGA II

L. Shi, B. Peng*

School of Mechanical & Electronical Engineering, Lanzhou University of Technology, Lanzhou, Gansu China

P A P E R I N F O	*A B S T R A C T*
	Adjusting the operating parameters to optimize the performance of the scroll expander has been a hot research topic among scholars. This paper innovatively combines the response surface method and NSGA2 algorithm for parameter optimization. This novel method can accurately predict the optimal operating parameters of the scroll expander and improve the overall efficiency of the scroll expander. Initially, a three-dimensional transient simulation model of the scroll expander was established, and the effects of three key operating parameters (suction pressure, exhaust pressure, and rotational speed) on the output power and isentropic efficiency of the scroll expander were analyzed through numerical simulation. On this basis, the response surface model between the input parameters and the objective function was established by using the response surface methodology. Consequently, three different optimization algorithms were compared, and it was found that NSGA-II had a better performance both in terms of convergence and solution performance,. Threfore, the NSGA-II algorithm was used for the multi-objective optimization. Under the premise of considering the maximum output power and isentropic efficiency, based on the established response surface model, the Pareto optimal solution was used to determine the optimal combination of its operating parameters: suction pressure of 1.62 MPa, exhaust pressure of 0.45 MPa, and rotational speed of 2,099.58 rpm.Finally, the numerical model is verified by the laboratory-built test bed of the Organic Rankine cycle low-temperature waste heat oil-free power generation system. The experimental results match well with the numerical simulation results and verify the model accuracy. The results from this pioneering and thorough thr study will provide a solid benchmark for the development and refinement of upcoming scroll machines. *doi*: *10.5829/ije.2024.37.01a.13*

1. INTRODUCTION

With the intensive research on scroll expanders, many scholars have attempted to improve the performance of scroll expanders by changing the geometry. Fanti et al. (1) investigated tooth side gap size on the features of vortex expanders. Alshammari et al. (2) used new mathematical models to improve the scroll expander's profile. Gao et al. (3) developed a new expander. It was shown that this design has better performance than conventional expanders.

As Computational Fluid Dynamics technology continues to evolve, the investigation into the internal flow field within the expander is garnering increasing interest among academic researchers. Feng et al. (4)

used the custom way to solve the vortex motion problem. Emhardt et al. (5) constructed a Vortex Swellers with variable wall thickness. Emhardt et al. (6) used new way to analyze the effect of variable Vortex Swellers. Zheng et al. (7) investigated the effect of the resolution of the CO_2 property table on the numerical simulation. Song et al. (8) proposed a symmetric exhaust structure of Vortex Swellers. Singh et al. (9) proposed symmetric exhaust structure of a Vortex Swellers. Song et al. (10) performed three-dimensional numerical simulations of a Vortex Swellers with different suction port positions based on CFD. Du et al. (11) compared the performance differences between T-CO_2 and R123. CO_2 and R123 performance differences, T-CO_2 exhibited better performance with an average isentropic efficiency 14% higher than that of R123.

*Corresponding Author Email: pengb2000@163.com (B. Peng)

With improvement of experimental conditions, more and more scholars also focus on the experimental study of vortex expanders. Zhang et al. (12) conducted an experimental study of vortex expanders at 65C-96°C and compared the effects of the work mass, Fatigati et al. (13) compared the difference in the performance of vortex expander and slide rotary expander on ORC respectively. Hsieh et al. (14) developed a new ORC using R123a as the work material and experimentally investigated the performanceof expander. Oh et al. (15) developed a new model of a Vortex Swellers, and through the coupling of the simulation model with the experimental vales, two key unknown parameters were identified. Jalili et al. (16) conducted research on the effect of carbon nanotube (CNT) particles on refrigeration cycle performance. They conducted specific and rigorous experiments. Vanaei et al. (17) conducted an evaluation and refinement of an altered incineration facility through the Organic Rankine Cycle.

Upon a thorough analysis of the research synopsis presented above, it can be inferred that output power and isentropic efficiency serve as pivotal metrics for assessing the operational efficacy of a scroll expander. These two key variables do not operate in a vacuum; instead, they are shaped by various factors, such as pressure, speed, and the distinct geometry of the scroll expander. Nevertheless, existing studies typically concentrate on examining the impact of a solitary factor on the performance of Vortex Swellers, leaving a noticeable gap in the comprehensive discussion on the adjustment of these operating parameters for performance optimization. Consequently, this study employs numerical simulation to conduct an all-encompassing investigation of the three operating parameters of Vortex Swellers, aiming to identify optimal parameters for real-world operation. Most notably, we introduce a novel optimization method, which combines the response surface methodology and the NSGA II algorithm to facilitate in-depth multi-objective optimization. This approach allows us to derive optimal operating parameters for the Vortex Swellers. The findings from this innovative and comprehensive study will offer a robust reference point for the design and enhancement of future scroll machines.

2. MODELING

2. 1. Geometric Modeling of a Vortex Expander
The design of the Vortex Swellers's profile is informed by circular involutes, with the tooth head correction relying on double arc correction. Figure 1 provides a visual representation of the Vortex Swellers's geometric model, while Table 1 lays out the specific geometric parameters in detail.
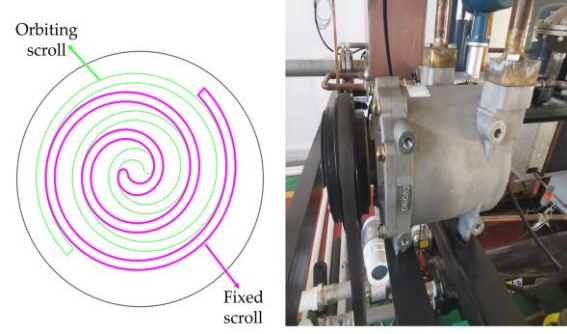

Figure 1. Geometric model of vortex expander

TABLE 1. Scroll expander geometric parameters

Definition	Parameters	Units	Value
Base circle radius	R	mm	4.647
Center distance	r	mm	9.6
Height of tooth	h	mm	42.5
Wall thickness	t	mm	5
Involute angle	a	°	30.767

2. 2. Turbulence Model
The continuity equation can be obtained by the following formulas (18).

$$\frac{\partial \rho}{\partial t} + \frac{\partial \rho u}{\partial x} + \frac{\partial \rho v}{\partial y} + \frac{\partial \rho w}{\partial z} - S_{add} = 0 \tag{1}$$

where P denotes mass per unit volume, t signifies temporal duration and u、v、w are speeds corresponding to the x、y、z axis, respectively. S_{add} embodies the accumulated mass in the continuous and any custom-defined origins. with a default value of 0.

The energy conservation equation can be obtained by the following formulas (19).

$$\frac{\partial}{\partial t}\left(\rho\left(U + \frac{v^2}{2}\right)\right) + \nabla\cdot\left(\rho v\left(h + \frac{v^2}{2}\right)\right) =$$
$$\nabla\cdot\left(\lambda_{eff}\nabla T - \sum_j h_j \vec{J}_j + \tau_{eff}\cdot\vec{v}\right) + S_{volume} \tag{2}$$

$$U = h - \frac{p_{op} + p}{\rho}, h = c_p dT + \frac{p}{\rho} \tag{3}$$

where λ_{eff} signifies the efficient transfer capacity, $\vec{J}_j$ alludes to the dispersion flow of the compound, U characterizes the intrinsic energy within the compound, h marks the perceptible heat content, τ_{eff} highlights the tension matrix, p_{op} pertains to the functional atmospheric force, P is the relative atmospheric force, and S_{volume} designates the bulk warmth origin.

2. 3. Vortex Expander Output Characteristics
Equation for the output power of Vortex wellers (20):

$$\overline{M} = \int_t^{t+T} M_t(t)dt = \int_t^{t+T} F_t \cdot r dt \tag{4}$$

$$W = \frac{2\pi n}{60} \overline{M} \tag{5}$$

where n signifies the spin frequency, $\overline{M}$ stands for the averaged momentum over time of the circulating scroll, F_t is the tangential force on the moving scroll disk, and r alludes to the foundational circle's diameter.

Equation for the isentropic efficiency of a vortex expander can be obtained by the following formulas (21):

$$\eta = \frac{H_1 - H_2}{H_1 - H_2'} = \frac{W}{\overline{m}(h_{in} - h_{out})} \tag{6}$$

where $\overline{m}$ represents the weight flux of the operational liquids over a time interval, h_{in} designates the articular heat content at the entry point of these liquids, and h_{out} points to the particular heat content at the exit point of these operational liquids.

2. 3. Meshing   The role of meshing is particularly important in computational fluid dynamics (CFD) analysis, which largely determines the accuracy and convergence of subsequent numerical simulations. ANSYS Fluent software will be used to perform numerical simulations. Taking the vortex expander as an example, a specific meshing strategy can effectively characterize the fluid region model of the vortex expander. Typically, a hybrid meshing strategy is used to model the fluid region of a vortex expander. This hybrid meshing approach is designed to maximize the reflection of the fluid flow characteristics inside the vortex expander. Figure 2 illustrates the mesh model.

2. 4. Grid Sensitivity Validation   In order to select the appropriate grid scale and number of computational domain grids, the numerical calculation results of five different numbers of grid models for
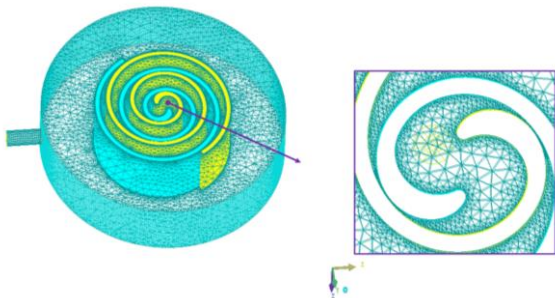
specific operating conditions were compared and the results are shown in Table 2. When comparing A3 grid to A1 grid and A2 grid , we found that their deviations in mass flow rate, driving moment and isentropic efficiency are less than 6%. While comparing the A3 grid to the A4 grid and A5 grid, we can observe that the deviations in mass flow rate, driving moment and isentropic efficiency are less than 8%. Considering the accuracy and efficiency together, A3 grid has met the requirements of grid independence and computational accuracy when performing the numerical simulation of the vortex expander.

3. ANALYSIS OF RESULTS

3. 1. Effect of Different Exhaust Pressures on the Performance of Scroll Eexpanders   We selected four distinct exhaust pressures for examination, with Table 3 detailing the specific working conditions associated with each other.

Figure 3 portrays the changes in isentropic efficiency and exported energy of the scroll expander under varying exhaust pressures. A close examination of Figure 3 reveals that an increase in exhaust pressure results in divergent trends for output power and isentropic efficiency. Specifically, exported energy decreases while isentropic efficiency increases. This is linked to the fact that the scroll expander's exported energy is influenced by the pressure differential between the inlet and outlet. An increase in exhaust pressure reduces this differential.

TABLE 2. Time-averaged performance of vortex expanders with different number of grids

Grid level	Total number of grids	Mass flow (kg/s)	Torques (N.m)	Isentropic efficiency (%)	Times (s)
A1	55E+4	0.11658	5.12	36.52	8h
A2	85E+4	0.12458	5.42	37.82	16h
A3	110E+4	0.12796	5.64	38.16	23h
A4	150E+4	0.13124	5.83	38.64	33h
A5	210E+4	0.13216	5.89	38.94	44h

TABLE 3. Different exhaust pressure parameters

Condition number	Suction pressure (MPa)	Inlet temperature (K)	Exhaust pressure (MPa)	Rotation speed (r/min)
S1	1.2	400	0.15	2000
S2	1.2	400	0.3	2000
S3	1.2	400	0.45	2000
S4	1.2	400	0.6	2000

Figure 2. Meshing model

Consequently, with a smaller pressure difference, the gas's capability to transform energy into mechanical work during expansion is restricted, leading to a reduction in the vortex expander's output power. On the other hand, a higher exhaust pressure decreases the pressure drop, which facilitates a more efficient conversion of pressure energy into kinetic energy. In addition, a moderate exhaust pressure helps to maintain a more stable flow velocity distribution and reduces the energy loss due to turbulence. In the actual expansion process, irreversible losses occur due to friction, turbulence, and non-uniform distribution of fluid pressure, leading to an increase in entropy (22). When the exhaust pressure is moderately increased, these irreversible losses are reduced; thus, increasing the isentropic efficiency.

The transient variation of the exported energy of the scroll expander at different exhaust pressures is given in Figure 4. Exported energy transient curve shows a downward flat trend Upon increasing the exhaust pressure as it goes from 0.15 MPa to 0.60 MPa. The exhaust pressure significantly affects the degree of gas expansion within the vortex expander, which in turn affects the output power. At lower exhaust pressures, the gas has to undergo a greater degree of expansion, releasing more energy and leading to an increase in output power. Conversely, at higher exhaust pressures, the gas expands less, releasing less energy and reducing the power output. Therefore, the magnitude of fluctuations in the output power transient plots and the average exported energy may vary under different exhaust pressure conditions.

3. 2. Effect of Different Suction Pressures on the Performance of Vortex Expanders
We maintained a constant inlet temperature for the Vortex Swellers's working mass, while varying the suction pressure. Table 4 presents the parameters pertaining to these simulated working conditions.
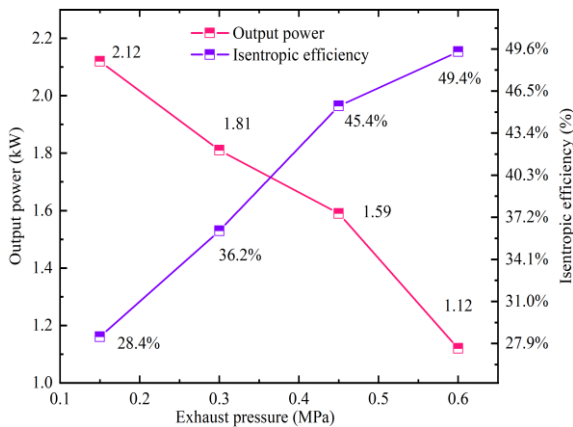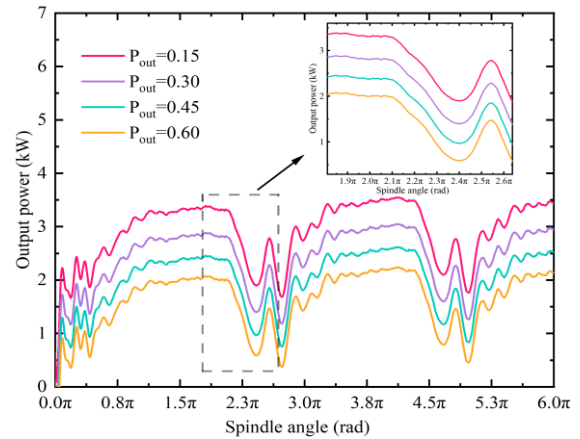

Figure 4. Variation of output power under different exhaust pressure

TABLE 4. Different suction pressure parameters

Condition number	Suction pressure (MPa)	Inlet temperature (K)	Exhaust pressure (MPa)	Rotation speed (r/min)
T1	0.8	400	0.25	2000
T2	1.1	400	0.25	2000
T3	1.4	400	0.25	2000
T4	1.7	400	0.25	2000

As latter escalates from 0.8 MPa to 1.7 MPa, the former sees a clear upward trend, moving from 1.074 kW to 3.056 kW. The underlying reason for this trend is the increased gas density with the rise in suction pressure. This enables Vortex Swellers to extract more energy from the gas, leading to an increment in output power. Figure 5 shows the isentropic efficiency and output power for different suction pressure. When assessing the isentropic efficiency in relation to suction pressure, a subtle increase is noticed as the suction pressure moves from 0.8MPa to1.1MPa. In contrast,
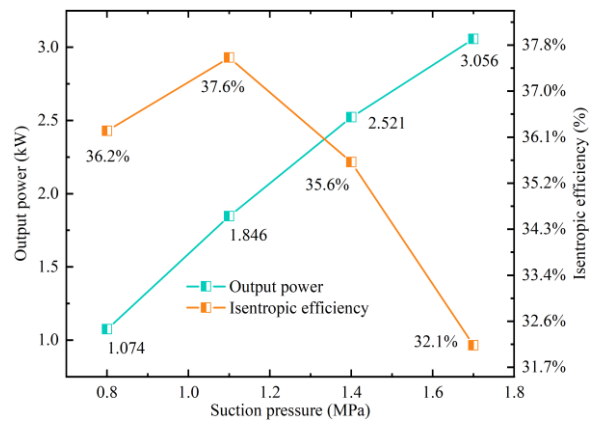

Figure 3. Isentropic efficiency and output power diagram for different exhaust pressure

Figure 5. Isentropic efficiency and output power for different suction pressure

between 1.1MPa and 1.7MPa, the isentropic efficiency reveals a decline, falling from 37.6% to 32.1% - a total reduction of 5.5%.

Figure 6 illustrates the temporal changes in the Vortex Swellers 's output power at various suction pressures. It is evident from the figure that the output power increases in line with the rise in suction pressure. This allows more fluid to participate in the expansion process per time unit, leading to a greater conversion of pressure energy into rotational energy in the moving scroll disk, and thereby enhancing the scroll expander's output power.

3. 3. Effect of Different Rotational Speeds on the Behavior of Vortex Expanders

Specific parameters are shown in Table 5.

An inspection of Figure 7 reveals that within the speed range of 1200rpm-2100rpm. The output power escalates from 1.27kW to 2.07Kw, marking a growth rate of 62.9%, whereas the isentropic efficiency moves up from 25.5% to 37.7%, indicating a growth rate of 47.8%.

Figure 8 provides the transient diagrams of the scroll expander's energy output at varying speeds. A perusal of Figure 8 reveals that at lower speeds, the export of energy experiences less fluctuation in the range of 1.9π to 2.2π, maintaining an overall steady trajectory. However, at higher speeds, the output power exhibits t
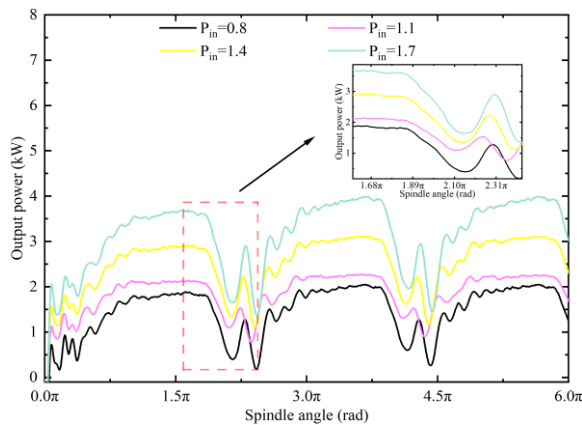

Figure 6. Transient curve of output power at different suction pressure

TABLE 5. Different exhaust pressure parameters

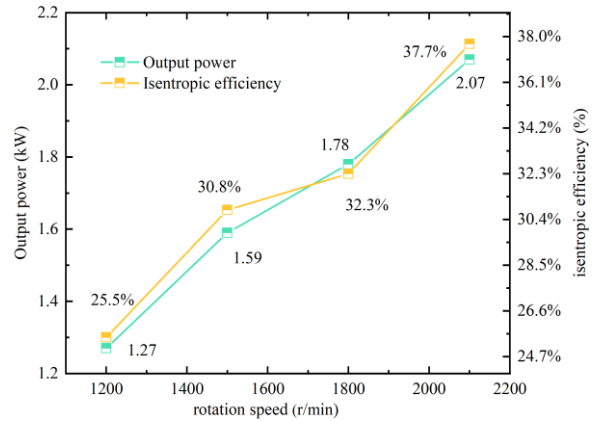| Condition number	Suction pressure (MPa)	Inlet temperature (K)	Exhaust pressure (MPa)	Rotation speed (r/min)
1	1.2	400	0.25	1200
2	1.2	400	0.25	1500
3	1.2	400	0.25	1800
4	1.2	400	0.25	2100

Figure 7. Graph of Isentropic efficiency and export of energy for different speeds
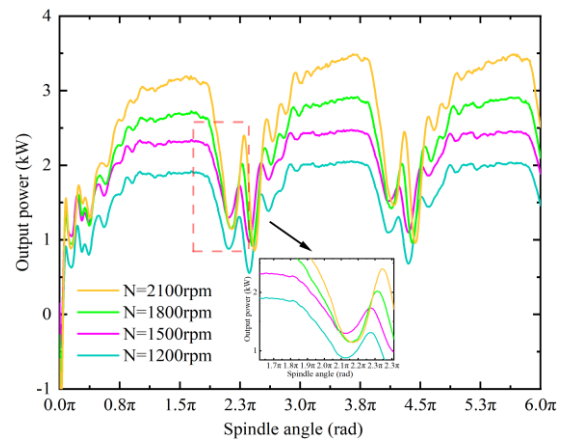

Figure 8. Transient diagram of output power at different speeds

more significan fluctuations, with a discernible downward trend. This can be attributed to the following reasons: In the scroll expander's low rotational speed phase, the gas expands slowly, resulting in a larger decrease in internal energy. This causes the export of energy to incrementally increase with the rise in rotational speed. As the Vortex Swellers moves into the mid-speed phase, the gas expansion speed picks up, the internal energy decreases, and the export of energy transient curve displays a slow growth, gradually stabilizing. However, in the high-speed phase, the gas expands too quickly, and the reduction in internal energy is limited. This results in the output power reaching a peak as the speed increases, after which an evident decline is observed.

4. MULTI-OBJECTIVE OPTIMIZATION

4. 1. Response Surface

Its main function is to form a response function that characterizes in detail the

interrelationships between input and output variables. This objective function can usually be expressed as an equation of the following form:

$$Y_i = \beta + \sum_{i=1}^{k} \beta_i x_i + \sum_{i=1}^{k} \beta_{ii} x_{ii}^2 + \sum_{i=1}^{k} \sum_{j>1}^{k} \beta_{ij} x_i x_j \tag{7}$$

We chose to adopt BBD for the experimental design of this study. Table 6 lists the parameters of BBD design.

4. 1. ANOVA and Regression Models

The magnitude of F-value is opposite to the magnitude of P-value. As shown in the Table 8, F of the model is 237.5 and P is less than 0.0001, these values indicate that the significance of our constructed model is very strong. In assessing the accuracy of the model, R^2 and R_{adj} important reference indicators. The closer the values of these two metrics are to 1 and the smaller the gap between them is, it means that the model is more

accurate. In the table, R^2 is 0.9967 and R_{adj} is 0.9925, which are both very close to 1, and the difference between them is only 0.0042, these values fully indicate that our model has a very high accuracy. From Table 9 we can find that R^2 is 0.9913 and Radj is 0.9807, both which are close to 1, highlighting the model's ability to accurately reflect changes in isentropic efficiency. At the same time, the small difference of only 0.0106 strongly confirms the high accuracy of the model.

The fitted curves are expressed as Equations 8 and 9.

$$W = -0.5636 + 1.1353A - 0.3088B - 0.001C + 0.8449AB + 0.0009AC - 0.004BC - 0.3835A^2 - 2.9686B^2 + 1.0833e-8C^2 \tag{8}$$

$$\eta = -0.2366 - 0.3676A - 0.3938B + 0.0002C + 0.2769AB - 0.0024AC + 0.0006BC - 0.1135A^2 - 0.9037B^2 - -5.7451e - 8C^2 \tag{9}$$

4. 2. Response Surface Result Analysis

In the response surface plot shown in Figure 9, we can find that the output power is at a low level at the combination of horizontal intervals of suction pressure taking the value range of 0.8-1.2 MPa and exhaust pressure taking the value range of 0.5-0.6 MPa. However, the output power is at a high level at the combination of horizontal intervals for the range of values of suction pressure 1.6-1.8 MPa and the range of values of exhaust pressure 0.15-0.3 MPa.

TABLE 6. Three-factor design table

Code	Variables	Level		
		-1	0	1
A	Suction pressure	0.8	1.3	1.8
B	Exhaust pressure	0.15	0.375	0.6
C	Rotation speed	1200	1600	2100

TABLE 7. Three-factor, three-level parameter design table

3	Suction pressure (MPa)	Exhaust pressure (MPa)	Rotation speed (r/min)	Output power (kW)	Isentropic efficiency (%)
	A	B	C		
S1	0.8	0.4	2000	0.683	40.5
S2	1.3	0.375	2000	2.312	33.4
S3	1.3	0.4	1600	1.599	37.9
S4	1.8	0.15	1600	2.736	26.1
S5	1.8	0.4	1300	2.033	30.3
S6	1.8	0.6	1600	1.999	38.6
S7	1.8	0.4	2000	2.982	40.6
S8	0.8	0.375	2000	1.074	36.2
S9	1.1	0.15	2000	1.843	37.6
S10	1.4	0.25	2000	2.504	35.6
S11	1.8	0.25	2000	3.053	32.1
S12	1.2	0.15	1600	2.123	28.4
S13	1.3	0.375	2000	1.811	36.4
S14	1.2	0.45	2000	1.591	45.5
S15	1.2	0.6	1200	1.095	49.4
S16	1.3	0.25	1200	1.276	25.5
S17	1.2	0.15	1600	1.598	30.8

TABLE 8. Output power analysis of variance table

Source	Sum of Squares	df	Mean Square	F-value	p-value
Model	7.27	9	0.8074	237.35	<0.0001
A	0.6234	1	0.6234	183.26	<0.0001
B	0.1297	1	0.1297	38.14	0.0005
C	0.1054	1	0.1054	30.99	0.0008
AB	0.0052	1	0.0052	1.52	0.2576
AC	0.0255	1	0.0255	7.49	0.0291
BC	0.0004	1	0.0004	0.1238	0.7353
A^2	0.0152	1	0.0152	4.48	0.0720
B^2	0.0331	1	0.0331	9.72	0.0169
C^2	4.622E-06	1	4.622E-06	0.0014	0.9716
Residual	0.0238	7	0.0034		
Lack of Fit	0.114	10	0.0025		
Pure Error	0.001	1	0.0018	4.541	0.362
Cor Total	7.29	16			
R^2=0.9967		R_{adj}=0.9925		C.V%=3.07	

TABLE 9. Isentropic efficiencyanalysis of variance table

Source	Sum of Squares	df	Mean Square	F-value	p-value
Model	1474.36	9	147.43	91.43	< 0.0001
A-pin	16.28	1	16.28	1.11	0.3274
B-pout	216.86	1	216.86	13.19	0.0084
C-N	68.46	1	68.46	58.88	0.0001
AB	32.16	1	32.15	6.81	0.0349
AC	8.64	1	8.64	3.56	0.1013
BC	3.86	1	3.86	9.88	0.0163
A^2	2.68	1	2.68	16.41	0.0049
B^2	4.42	1	4.42	37.64	0.0005
C^2	6.46	1	6.46	1.60	0.2468
Residual	122.24	7	7.86		
Lack of Fit	120.68	11	9.48		
Pure error	0.12	1	0.18		
Cor Total	1842.68	16			
R^2=0.9916		R_{adj}=0.9807		C.V%2.55	

As shown in Figure 10, it can be found that the fluctuation of the surface in the direction of suction pressure is large, while the fluctuation of the surface in the direction of speed is relatively small. This indicates that the effect of suction pressure on the output power is more significant compared to the effect of rotational speed. This finding is important for practical applications because the researcher can maximize the output power by adjusting the combination of suction pressure and rotational speed. The output power falls in the optimum range when the suction pressure is 1.6MPa-1.8MPa and the rotational speed lies in the range of 1850-2000rpm.

Figure 11 demonstrates the response surface plots of the output power as a function of exhaust pressure and rotational speed. Observing Figure 11, we can find that when the exhaust pressure is in the range of 0.15MPa-0.33MPa, the trend of output power reduction is more obvious as the exhaust pressure decreases. However,
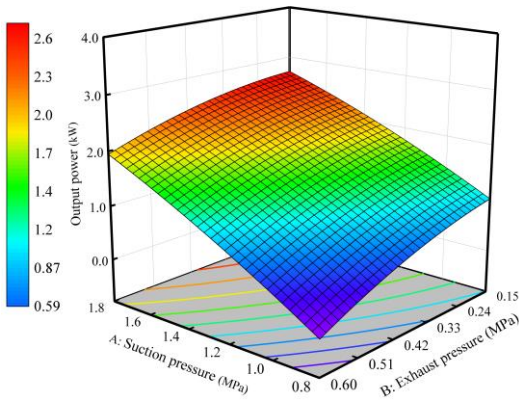
Figure 9. Response surface of output power under the interaction of suction pressure and exhaust pressure
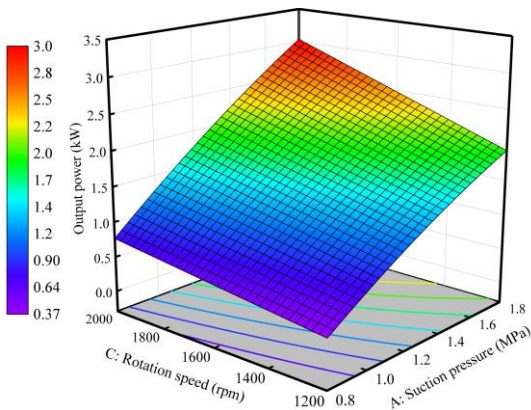

Figure 10. Response surface of output power under the interaction of suction pressure and rotational speed

when the exhaust pressure is at 0.33MPa-0.60MPa, the trend of output power reduction is relatively slower as the exhaust pressure decreases. This indicates that at different exhaust pressure intervals, the output power has different sensitivities to changes in exhaust pressure.
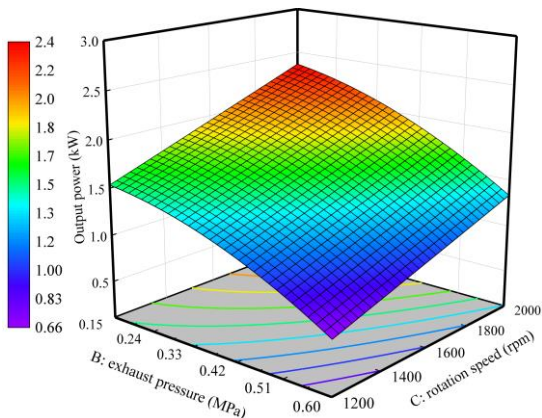

Figure 11. Response surface of output power under the interaction of exhaust pressure and rotational speed

The interaction between response surface and contour visuals, as depicted in Figure 12, demonstrates the trend of isentropic efficiency under varied inlet and exhaust pressure conditions. This analysis suggests that notable enhancement in isentropic efficiency can be achieved when the intake pressure is set between 1.6-1.8 MPa and the exhaust pressure falls within the 0.5-0.6 MPa range. This finding bears significant implications, serving as a valuable guide for optimizing the configuration of suction and exhaust pressures to boost the isentropic efficiency of the machinery in real-world applications.

The response surface as shown in Figure 13 reveals in detail the variation characteristics of isentropic efficiency under different conditions of intake pressure and rotational speed. Based on the data analysis in Figure 13, we can conclude that the optimal performance interval of isentropic efficiency is concentrated in the range of 1.1-1.3 MPa intake pressure and 1800-2000 rpm rotational speed under the consideration of only two influencing factors, namely, intake pressure and rotational speed.

The response surface shown in Figure 14 reflects the changing law of isentropic efficiency under different
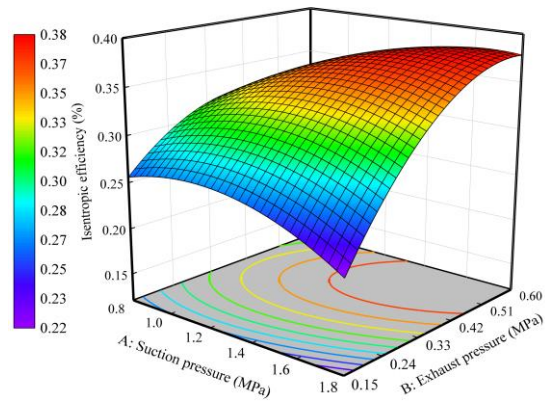

Figure 12. Isentropic efficiency response surface under the interaction of suction pressure and exhaust pressure
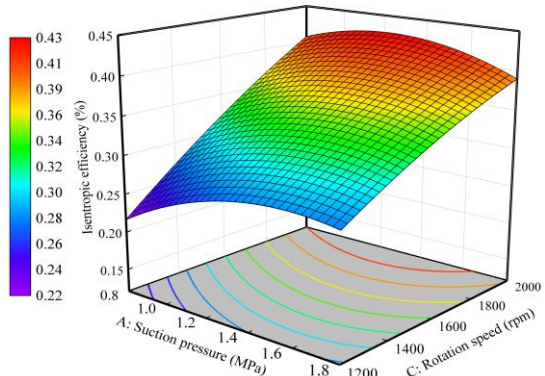

Figure 13. Isentropic efficiency response surface for the interaction of suction pressure and rotational speed
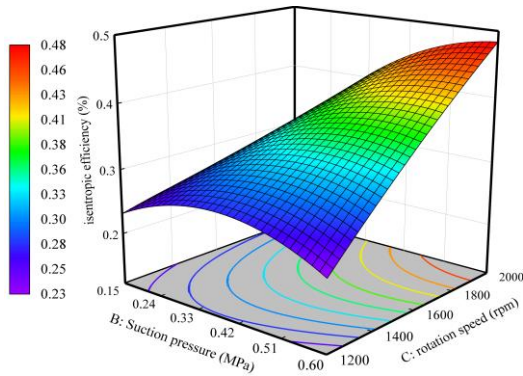
Figure 14. Isentropic efficiency response surface under the interaction of exhaust pressure and rotational speed

exhaust pressure and rotational speed conditions. We can conclude that the isentropic efficiency can reach the optimal parameter range when the exhaust pressure is about 0.51-0.6 MPa and the rotational speed is in the range of 1600-2000 rpm.

4. 3. Performance Comparison of Algorithms

To identify the best operational parameters, this research contrasts three frequently employed multi-objective optimization algorithms (MOPSO, NSGA-II, MOEA/D). Eventually, we settle on the NSGA-II algorithm as the most compatible with our model. Figure 15 provides the Pareto optimal solution set diagrams for the three optimization algorithms. The allocation of decision variables for these three optimization algorithms is depicted in Figure 16. From Figure 15, the NSGA-II algorithm has a more concentrated non-inferior solution set and a better diversity of solutions, and the solution set covers all regions of the solution space, which means that we can choose between solutions to satisfy different priorities and preferences. Algorithms with centralized and dense non-inferior solution sets tend to have better convergence. This means that the algorithms are able to find better solutions in a shorter time, which improves the efficiency of solving the optimization problem.

From Figure 16, the MOPSO algorithm as a whole has a more decentralized distribution of decision variables, which presents an unconcentrated character. This means that in the solution space, the MOPSO algorithm is not able to search better for excellent solutions in multiple regions, and the convergence and diversity performance is average (23). The NSGA-II has a fairly uniform distribution of decision variables on the whole, and exhibits better convergence. This indicates that the algorithm is able to effectively find a set of excellent solutions in the solution space with a strong search capability. Compared to the other two algorithms (NSGA II and MOPSO), the MOEA/D algorithm has a wider distribution of decision variables on exhaust pressure, which is mainly concentrated in the range of 0.1MPa-0.55MPa. This implies that the algorithm has a more comprehensive search capability in the exhaust pressure direction and is able to find more potentially excellent solutions. However, in the direction of suction pressure, the distribution of decision variables of the MOEA/D algorithm does not perform well.

In order to better and comprehensively evaluate the advantages and disadvantages of the three algorithms, we introduced HV, IGD, and computation time at the same time for comprehensive evaluation, and the values of the specific evaluation indexes are given in Table 10. Larger HV values and smaller IGD values indicate better performance of the algorithms, and we can see from the table that NSGA-II has obvious advantages over the other two algorithms in terms of HV, IGD, and computation time.

Equation 10 gives the range of values of the independent variables, and for subsequent optimization, the result of the NSGA-II algorithm are given Table 11.

$$\begin{cases} Maximize : \text{output power} = f_1(P_{in}, P_{out}, n); \\ Maximize : \text{Isentropic efficiency} = f_2(P_{in}, P_{out}, n). \\ 0.8\text{MPa} \leq P_{in} \leq 1.8\text{MPa} ; \\ 0.15\text{MPa} \leq P_{out} \leq 0.6\text{MPa}; \\ 1200\text{rpm} \leq n \leq 2100\text{rpm}. \end{cases} \quad (10)$$
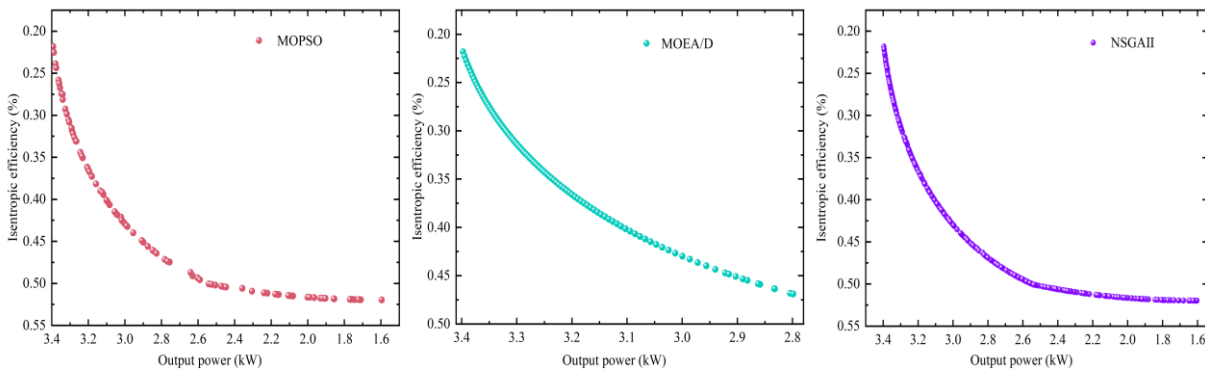

Figure 15. Non-inferiority solution set diagram of three multi-objective optimization algorithms
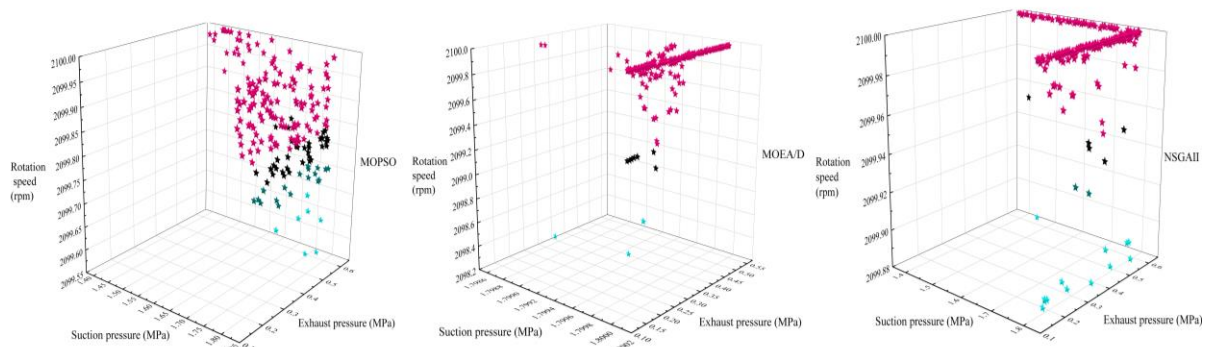
Figure 16. Distribution of decision variables for three multi-objective optimization algorithms

TABLE 10. Table of performance indicators of the three algorithms

Algorithms	HV	IGD	calculation time (s)
MOPSO	0.9168	1.7569	12.96
NSGA-II	0.9412	1.6686	8.59
MOEA/D	0.9356	2.4214	51.86

TABLE 11. Main parameters of NSGA-II algorithm

Parameters	Values
Population size	150
Crossover probability	0.9
Mutation probability	0.02
Maximum generation size	500

By running the NSGA-II algorithm, we obtained a set of Pareto solutions as shown in Figure 17. This set of solutions demonstrates the trade-offs between different objective functions, thus providing diversified choices for decision makers. Point C in Figure 17 is the desired ideal point, where the output power is 3.02 kW, the efficiency is 42.6%, and the optimal operating parameters are: suction pressure is 1.62 MPa, exhaust pressure is 0.45 MPa, and the rotational speed is 2099.58 rpm. The optimal operating parameters solved by the NSGA II algorithm are compared with the simulated values to determine the accuracy of the solution, and the results in Table 12. gives the comparison results. From Table 12, the predicted value of the output power solved by the NSGA II algorithm is

3.02 kW, and the simulated value calculated by numerical simulation is 3.16 kW, with a deviation of 4.4%, and the predicted value of the isentropic efficiency is 42.6%, and the simulated value is 45.4%, with a deviation of 6.2%. The deviation of both is less than 8%, which shows the high accuracy of the optimal solution

5. EXPERIMENTAL VALIDATION

To validate the reliability of the vortex expander's numerical simulation outcomes, we juxtaposed the predicted data with the findings from our experimental setup. Figure 18 provides an intricate depiction of the testing platform. At the heart of this setup is the scroll expander, adapted from an oil-free scroll compressor.
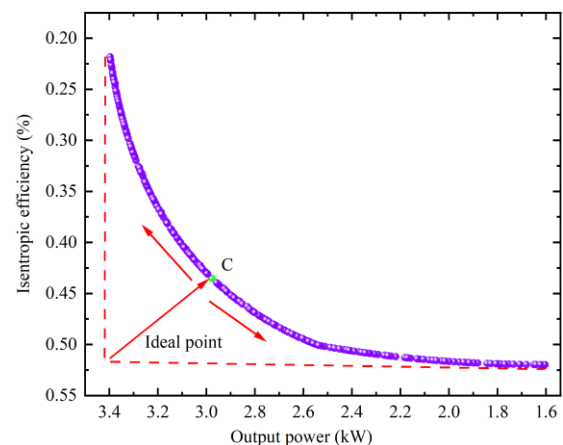

Figure 17. Pareto front plot of NSGA II algorithm

TABLE 12. Comparison of predicted values and simulations

Suction pressure (mpa)	Exhaust pressure (mpa)	Rotation speed (rpm)	Output power (kw)		Isentropic efficiency (%)	
			Predicted value	Simulated value	Predicted value	Simulated value
1.62	0.45	2099.58	3.02	3.16	42.6	45.4

Complementing this, the apparatus incorporates a specialized mass flow pump. It's further outfitted with an evaporator and condenser, each tasked with the vaporization and liquefaction of the working mass, respectively. For precise oversight, we have integrated a smart electromagnetic flow meter. This instrument continuously captures the mass flow rate, enabling meticulous oversight and precision throughout the experimentation phase.

To calibrate the measuring equipment, the following preparations are made:

(1) Make sure that the components of the ORC system are installed and well connected. Make sure the voltmeter is connected correctly and securely to avoid errors or accidents. Connect the ammeter in series with the generator output circuit. Typically, this means that the circuit needs to be disconnected and the two probes of the ammeter connected at each end of the disconnect. Make sure the ammeter is properly and securely installed during installation.

(2) System initialization and preheating: Start the work pump to circulate the work through the system. Start the heater and gradually increase the temperature of the evaporator to evaporate the work mass. During this process, pay attention to monitor the readings of each measuring instrument to ensure that the working parameters are within the safe range.

(3) Adjustment of suction pressure: Before starting the experiment, select the appropriate suction pressure according to the expected test range. The inlet pressure can be changed by adjusting the frequency of the work pump

(4) After adjusting the suction pressure, wait for the system to reach a stabilized condition. During this time, continuously monitor the readings of each measuring instrument to ensure that the operating parameters remain within the expected range. At the same time, record the suction pressure, temperature, and other parameters of scroll expander at this time.

Figure 19 depicts the schematic diagram of the experiment. The test implementation process strictly adheres to the provisions in the Organic Rankine Cycle Power Generation Unit (JB/T13305-2017)

All experimental data are averaged over several measurements to ensure the reliability of the data.

Firstly, we adjust the inlet pressure into the vortex expander by changing the operating frequency of the work pump.
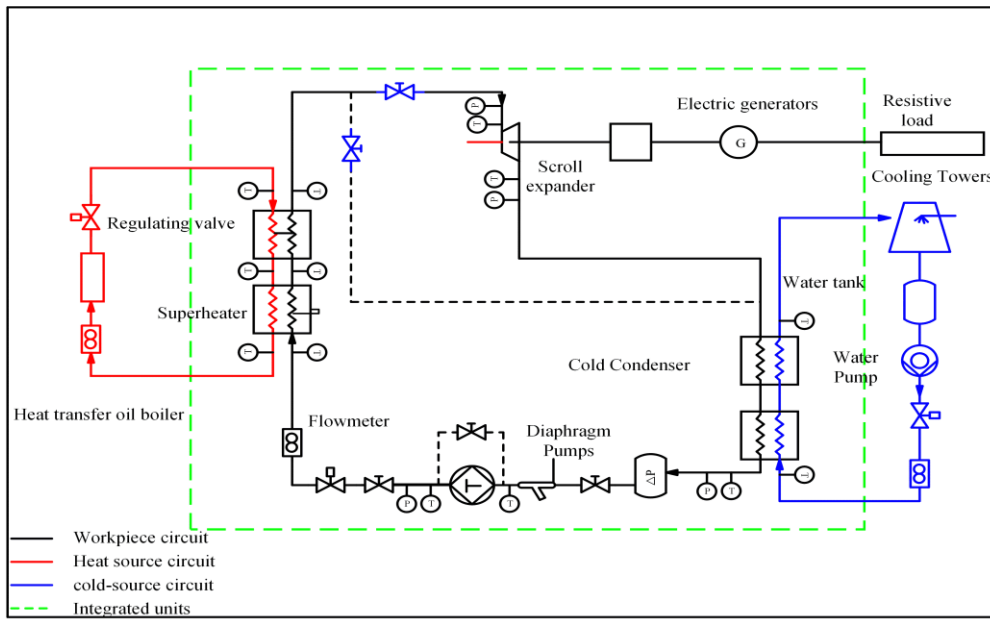

Figure 18. Experimental platform diagram

Figure 19. Experimental schematic

Secondary, we monitor in real time the voltage and current flowing through the scroll expander. Based on these parameters, we can calculate the export of energy of the scroll expander.

Finally, we compare experimental output power values at different inlet pressures with the simulated values.

Figure 20 shows the experimental values of voltage and current flowing through the scroll expander at different inlet pressures, as measured by our experimental platform. These data are an important basis for analyzing and understanding the operating conditions of the scroll expander.

Figure 21 shows the experimental and simulated output power values. The maximum deviation in output power is 10.86% at a suction pressure of 1.1 MPa. Overall, the deviation between the simulated and experimental results is between 3% and 11%, which constitutes a relatively small deviation. This indicates that model we established is relatively accurate and can effectively simulate the operating characteristics of the scroll expander under different operating conditions.

 Meanwhile, we also measured the experimental and simulated values of isentropic efficiency. Figure 22 shows the experimental and simulated values of isentropic efficiency at different suction pressures. The maximum error occurs when the inspiratory pressure is 0.8 MPa, and the maximum error is 12.7%. The reasons for this deviation may be the existence of certain errors in the actual measurement process, the friction loss of the machine and other factors.
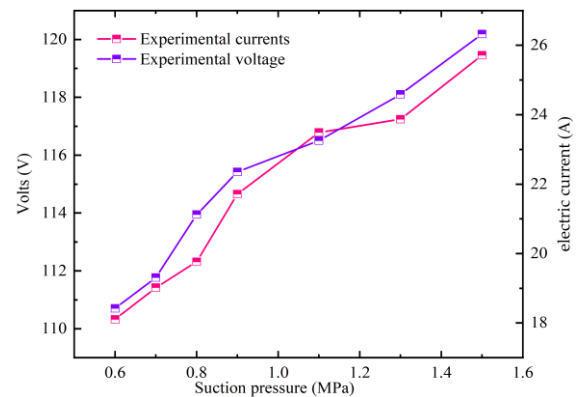

Figure 20. Experimental current-voltage diagram at different suction pressures
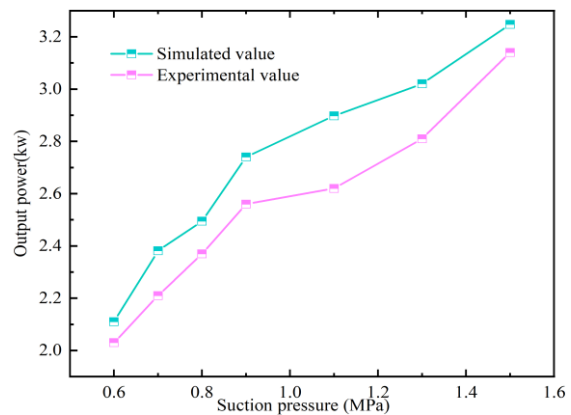

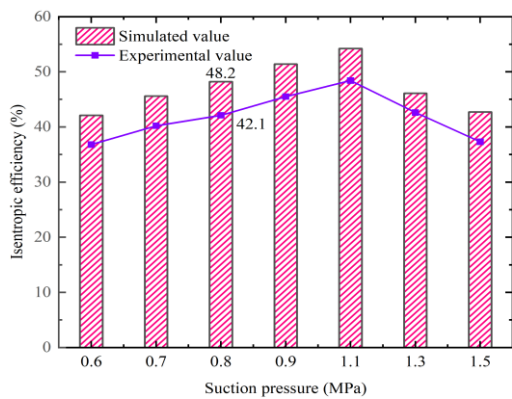**Figure 21.** Simulated versus experimental values of output power

Figure 22. Experimental and simulated values of isentropic efficiency at different suction pressures

6. CONCLUSION

Distinct from the research undertakings of prior scholars regarding the operational parameters of the scroll expander, the majority have primarily focused on discerning the extent to which these parameters impact the generated energy and adiabatic effectiveness of the device. Significantly, some academics have deliberated on the optimal configuration of these parameters to ensure peak performance of the scroll expander. This study introduces a methodological fusion of the response surface technique and the NSGA-II algorithm, achieving the optimal operational parameters for the scroll expander. Under these parameters, the scroll expander's performance is comprehensively maximized. The accuracy of this innovative approach has been rigorously validated using a specially constructed experimental platform. Renowned for its high precision and rapid problem-solving capabilities, this novel methodology presents a fresh theoretical framework and perspective for the optimization of the scroll expander. The specific conclusions are as follows:

(1) As the exhaust pressure increases, the pressure difference at the inlet side of the scroll expander decreases, resulting in a lower mass flow rate at the inlet side. Due to the internal structure of the scroll expander, the mass flow rate at the outlet side remains essentially the same as the mass flow rate at the inlet side. A rise in exhaust pressure from 0.15 MPa to 0.60 MPa leads to contrasting trends in the generated energy and adiabatic effectiveness: there's a reduction in output power by 47.17%,while the isentropic efficiency surges by 73.94%. The output power shows a linear increase with the increase of suction pressure. An increase in suction pressure from 0.8 MPa to 1.7 MPa results in a rise in output power by 1.982 kW.the isentropic efficiency shows an initial increase and then a decrease due to factors such as friction and turbulence. When the speed is in the range of 1200 rpm to 2100 rpm, both the isentropic efficiency and the output power increase with the increase in speed.

(2) The NSGA-II algorithm is more suitable for the multi-objective optimization model both in terms of convergence and solution performance. The maximum export power and isotropy efficiency of the Vortex Expander are derived from solution to be 3.02 kW and 42.6%, respectively, with deviations of 4.4% and 6.2% from the simulated values. The optimum operating parameters: suction pressure, exhaust pressure and rotational speed were 1.62MPa, 0.45MPa and 2099.58rpm.

(3) The accuracy of our method is verified by the organic Rankine cool thermal waste energy production system built in laboratory. The maximum deviations of the experimental values of export power and isotropy efficiency from simulated values are 10.86% and 12.7%, respectively, and the errors are lower than 13%, indicating that the method has relatively better accuracy and can be applied to the actual manufacture. The reasons for this deviation may be the existence of certain errors in the actual measurement process, the friction loss of the machine and other factors.

7. REFERENCES

1. Fanti GR, Romo DA, Almeida RD, Mello PD. Influence of flank clearance on the performance of a scroll expander prototype. Energy. 2020;193.

2. Alshammari F, Pesyridis A, Elashmawy M. Turbine optimization potential to improve automotive Rankine cycle performance. Applied Thermal Engineering. 2021;186:116559. https://doi.org/10.1016/j.applthermaleng.2021.116559 https://www.sciencedirect.com/science/article/pii/S13594311210 00168

3. Gao J, Ma C, Tian G, Xing S, Jenner P. Numerical investigations of an opposed rotary piston expander for the purpose of the applications to a small-scale Rankine cycle. Applied Thermal Engineering. 2021;182:116157.

4. Xiao GF, Liu GP, Wang JT, Song HG, University N, University J. Three-dimensional Numerical Simulation for Transient Flow in a Scroll Compressor Using Dynamic Mesh Technique. Fluid Machinery. 2014.

5. Emhardt S, Tian G, Song P, Chew J, Wei M. CFD modelling of small scale ORC scroll expanders using variable wall thicknesses. Energy. 2020;199:117399. https://doi.org/10.1016/j.energy.2020.117399 https://www.sciencedirect.com/science/article/pii/S03605442203 05065

6. Emhardt S, Tian G, Song P, Chew J, Wei M. CFD analysis of the influence of variable wall thickness on the aerodynamic performance of small scale ORC scroll expanders. Energy. 2022;244. 10.1016/j.energy.2021.122586

7. Zheng S, Wei M, Song P, Hu C, Tian R. Thermodynamics and flow unsteadiness analysis of trans-critical CO2 in a scroll compressor for mobile heat pump air-conditioning system. Applied Thermal Engineering. 2020;175. 10.1016/j.applthermaleng.2020.115368

8. Song P, Wei M, Zhang Y, Sun L, Emhardt S, Zhuge W. The impact of a bilateral symmetric discharge structure on the

performance of a scroll expander for ORC power generation system. Energy. 2018;158:458-70. https://doi.org/10.1016/j.energy.2018.06.053 https://www.sciencedirect.com/science/article/pii/S0360544218311186

9. Singh S, Singh A, Dasgupta MS. CFD Modeling of a Scroll Work Recovery Expander for Trans-critical CO 2 Refrigeration System. Energy Procedia. 2017;109:146-52. 10.1016/j.egypro.2017.03.081

10. Song P, Wei M, Liu Z, Zhao B. Effects of suction port arrangements on a scroll expander for a small scale ORC system based on CFD approach. Applied Energy. 2015;150:274-85. 10.1016/j.apenergy.2015.04.046

11. Du Y, Tian G, Pekris M. Unsteady and three-dimensional computational fluid dynamics modelling of scroll expander for low-grade waste heat recovery transcritical carbon dioxide micro-scale power system. Energy Conversion and Management. 2023;282. 10.1016/j.enconman.2023.116857

12. Zhang H-H, Zhang Y-F, Feng Y-Q, Chang J-C, Chang C-W, Xi H, et al. The parametric analysis on the system behaviors with scroll expanders employed in the ORC system: An experimental comparison. Energy. 2023;268. 10.1016/j.energy.2023.126713

13. Fatigati F, Vittorini D, Coletta A, Cipollone R. Assessment of the differential impact of scroll and sliding vane rotary expander permeability on the energy performance of a small-scale solar-ORC unit. Energy Conversion and Management. 2022;269. 10.1016/j.enconman.2022.116169

14. Hsieh J-C, Chen Y-H, Hsieh Y-C. Experimental study of an organic Rankine cycle with a variable-rotational-speed scroll expander at various heat source temperatures. Energy. 2023;270. 10.1016/j.energy.2023.126956

15. Oh J, Jeong H, Kim J, Lee H. Numerical and experimental investigation on thermal-hydraulic characteristics of a scroll expander for organic Rankine cycle. Applied Energy. 2020;278. 10.1016/j.apenergy.2020.115672

16. Jalili B, Ghafoori H, Jalili P. Investigation of carbon nano-tube (CNT) particles effect on the performance of a refrigeration cycle. Int J Mater Sci Innov. 2014;2(1):8-17.

17. Vanaei P, Jalili B, Hosseinzadeh M, Jalili P. Efficiency Optimization Thermal Analysis and Power Output of a Modified Incinerator Plant Using Organic Rankine Cycle. International Journal of Engineering. 2023;36(7):1300-9.

18. Chang J-C, Chang C-W, Hung T-C, Lin J-R, Huang K-C. Experimental study and CFD approach for scroll type expander used in low-temperature organic Rankine cycle. Applied Thermal Engineering. 2014;73(2):1444-52. https://doi-org-s.lut.yitlink.com:443/10.1016/j.applthermaleng.2014.08.050 https://www-sciencedirect-com-s.lut.yitlink.com:443/science/article/pii/S1359431114007467

19. Feng Y-q, Xu J-w, He Z-x, Hung T-C, Shao M, Zhang F-y. Numerical simulation and optimal design of scroll expander applied in a small-scale organic rankine cycle. Energy. 2022;260:124981. https://doi-org-s.lut.yitlink.com:443/10.1016/j.energy.2022.124981 https://www-sciencedirect-com-s.lut.yitlink.com:443/science/article/pii/S0360544222018795

20. Feng Y-q, Liang H-j, Xu K, Wang Y, Lu Y, Lin C-H, et al. Experimental study on the performance of a great progress 10 kW organic Rankine cycle for low-grade heat source based on scroll-type expander. Energy. 2023;284:128627. https://doi-org-s.lut.yitlink.com:443/10.1016/j.energy.2023.128627 https://www-sciencedirect-com-s.lut.yitlink.com:443/science/article/pii/S0360544223020212

21. Narasimhan AK, Wickramaratne C, Kamal R, Goswami DY, Singh P. Mapping scroll expander performance for organic working fluids using dimensionless parameters in Ns-Ds diagram. Energy. 2019;182:739-52. https://doi.org/10.1016/j.energy.2019.06.054 https://www.sciencedirect.com/science/article/pii/S0360544219311831

22. Jalili B, Mousavi A, Jalili P, Shateri A, Domiri Ganji D. Thermal analysis of fluid flow with heat generation for different logarithmic surfaces. International Journal of Engineering. 2022;35(12):2291-6.

23. Shijing D, Hongru C, Xudong W, Deshi W, Yongyong Z. Modal Optimization Design of Supporting Structure Based on the Improved Particle Swarm Algorithm. International Journal of Engineering. 2022;35(4):740-9. 10.5829/ije.2022.35.04A.14 https://www.ije.ir/article_143223.html

---

Persian Abstract

چکیده

تنظیم پارامترهای عملیاتی برای بهینه‌سازی عملکرد گسترش‌دهنده اسکرول یک موضوع تحقیقاتی داغ در بین محققان بوده است. این مقاله به طور خلاقانه ای روش سطح پاسخ و الگوریتم NSGA2 را برای بهینه سازی پارامتر ترکیب می کند. این روش جدید می تواند پارامترهای عملیاتی بهینه گسترش دهنده اسکرول را با دقت پیش بینی کند و کارایی کلی گسترش دهنده اسکرول را بهبود بخشد. در ابتدا، یک مدل شبیه سازی گذرا سه بعدی از گسترش دهنده اسکرول ایجاد شد و اثرات سه پارامتر عملیاتی کلیدی (فشار مکش، فشار اگزوز و سرعت چرخش) بر توان خروجی و راندمان همسانتروپیک گسترش دهنده اسکرول از طریق عددی مورد تجزیه و تحلیل قرار گرفت. شبیه سازی. بر این اساس، مدل سطح پاسخ بین پارامترهای ورودی و تابع هدف با استفاده از روش سطح پاسخ ایجاد شد. در نتیجه، سه الگوریتم بهینه‌سازی مختلف با هم مقایسه شدند و مشخص شد که NSGA-II عملکرد بهتری هم از نظر هم‌گرایی و عملکرد حل دارد. بنابراین، الگوریتم NSGA-II برای بهینه‌سازی چند هدفه استفاده شد. با فرض در نظر گرفتن حداکثر توان خروجی و راندمان ایزنتروپیک، بر اساس مدل سطح پاسخ ایجاد شده، از راه حل پارتو بهینه برای تعیین ترکیب بهینه پارامترهای عملیاتی آن استفاده شد: فشار مکش 1.62 مگاپاسکال، فشار خروجی اگزوز 0.45 مگاپاسکال و سرعت چرخش 2,099.58 دور در دقیقه. در نهایت، مدل عددی توسط بستر آزمایشی ساخته‌شده در آزمایشگاه سیستم تولید برق بدون روغن حرارتی با دمای پایین چرخه ارگانیک رانکین تأیید می‌شود. نتایج تجربی به خوبی با نتایج شبیه‌سازی عددی مطابقت دارند و صحت مدل را تأیید می‌کنند. نتایج حاصل از این مطالعه پیشگامانه و کامل، یک معیار محکم برای توسعه و اصلاح ماشین‌های اسکرول آینده ارائه می‌کند.